Dynamics of multiphoton scattering in a two-level mixer

A. V. Vasenin ®,[1,2,*] A. Yu. Dmitriev ®,[2,†] S. V. Kadyrmetov ®,[2] A. N. Bolgar ®,[2] and O. V. Astafiev ®[1,2,3]

[1]*Skolkovo Institute of Science and Technology, Nobel Street 3, 143026 Moscow, Russia*
[2]*Laboratory of Artificial Quantum Systems, Moscow Institute of Physics and Technology, 141700 Dolgoprudny, Russia*
[3]*Physics Department, Royal Holloway, University of London, Egham, Surrey TW20 0EX, United Kingdom*

A superconducting qubit in a waveguide behaves as a pointlike nonlinear element. If irradiated with nearly resonant microwave pulses, the qubit undergoes quantum evolution and generates coherent fields at sideband frequencies due to elastic scattering. This effect is called quantum wave mixing (QWM), and the number of emerged side components depends on the number of interacting photons. By driving a superconducting qubit with short pulses with alternating carrier frequencies, we control the maximal number of photons simultaneously interacting with a two-level system by varying the number and duration of applied pulses. Increasing the number of pulses results in consecutive growth of the order of nonlinearity, which manifests in additional coherent side peaks appearing in the spectrum of scattered radiation while the whole spectrum maintains its asymmetry.

The scattering of electromagnetic waves on a single atom in an open space is a cornerstone problem in quantum optics [1–3]. A two-level system driven by resonant monochromatic tone is a great playground to create and study nontrivial light with sophisticated properties. In addition to the predicted [4,5] and later observed [6–8] intensity-dependent Rayleigh scattering and three-peaked inelastic spectrum, the scattered field exhibits direction- and power-dependent bunching [9] and antibunching [10–13], squeezing [14–17], sub-Poissonian photon statistics [18] and spectral correlations [19,20], and quantum amplification of probe signal [21]. Therefore, various aspects of resonance fluorescence are well studied, finding its applications in microwave photonics and quantum information processing platforms based on propagating fields. However, altering the drive to a pair of tones (so-called bichromatic drive) complicates the stationary and dynamic characterization of the field emitted by a dressed two-level system.

The pioneering experiments with atomic vapors [22], quantum dots [23], and superconducting qubits [24] revealed that an inelastic fluorescence spectrum under the bichromatic drive becomes qualitatively different from the well-known Mollow triplet for the monochromatic drive. In the case of symmetrically detuned drives (that is, located at $\omega_\pm = \omega_d \pm \delta\omega$, where ω_d is central frequency of drives, typically equal to qubit frequency ω_q, and $\delta\omega$ is arbitrary chosen detuning) with equal Rabi amplitudes $\Omega_- = \Omega_+ = \Omega$, the spectrum consists of many peaks. For any integer n there is a peak at $\omega_{\pm n} = \omega_d \pm n\delta\omega$, and these frequencies do not depend on the Ω of each drive but their intensities do. This effect was explained with the direct Bloch equation solutions [25,26], and in some works with the use of the dressed atom picture [27,28]. The elaborated theory gives correct peak positions and heights.

However, the *elastic* components predicted [27,29] to appear at $\omega_{\pm(2p+1)}$ for all integers p were hardly observed in traditional quantum optics, partially because coherent field measurements are rather cumbersome in optics of visible range [30] when compared with, for example, photocounting measurements. The only observation of elastic scattering known to us was made with a high-finesse Fabry-Perot cavity [23]. However, the method was not phase-sensitive and intensities of elastic components for different parameters were not analyzed. In contrast, the elastic field components are straightforwardly observed in microwave scattering by a single superconducting qubit in a waveguide [8,31,32]. Their emergence is analogous to the coherent optical wave mixing in nonlinear media, although the medium consists of the only two-level system. Thereby, the observed mixing is called the quantum wave mixing (QWM) [33–35], and it is efficient in the regime $\delta\omega \ll \Gamma_1$ and $\Omega_\pm \gtrsim \Gamma_1$. Moreover, it was proposed [34] and theoretically confirmed [36] that QWM could reveal photon statistics of nonclassical light in one of the modes. It could become a handy tool for microwave quantum optics: The absence of reliable photon detectors of sufficiently wide bandwidth and high efficiency is significant restriction for microwave waveguide photonics.

In the current work, we measure a complete picture of the QWM spectrum due to elastic scattering of microwave pulses when the qubit undergoes coherent dynamics. To achieve that, the qubit is driven by a series of N non-overlapping pulses with alternating frequencies ω_- and ω_+, with N from 2 to 6. In the elastic spectrum, we observe solely $2N - 1$ components which depend on the maximal number of interacting photons. Particularly, we extend the result of Ref. [33], where two pulses ($N = 2$) represented maximum three photon interaction and, therefore, a quantized spectrum consisted of three peaks only. We also measure the maps of complex amplitudes depending on the durations of blue- and redshifted pulses and fit them with analytical calculations, finding excellent agreement with the measurements. In addition, we

*vasenin.av@phystech.edu
†dmitrmipt@gmail.com

numerically find the evolution and characterize the dependence of the side peaks for the specific case of three partially overlapping pulses. Our results demonstrate a high degree of control of nonlinear light scattering on a single atom in the time domain. They will serve as a basis for the development of nonlinear quantum electronics with superconducting systems and for studying its transient properties under strong drive.

For the time-domain multiphoton QWM experiment, we utilize a single transmon qubit [37] as an artificial atom. The qubit consists of a shunting capacitor with the charging energy of $E_C/h = 309$ MHz and an asymmetric SQUID [38] with the total Josephson energy of $E_{J\Sigma}/h = (E_{J1} + E_{J2})/h = 17.0$ GHz and the junction asymmetry $d = 0.5$, giving the upper sweet spot resonance transition at $\omega_q/2\pi = 6.1$ GHz. The qubit is coupled to the central conductor of an on-chip coplanar waveguide with the effective capacitance $C_c = 9.6$ fF, which results in the waveguide-induced decay constant $\Gamma_1/2\pi = 1.64$ MHz in the upper sweet spot. The radiative decay to the free space is typically negligible; hence Γ_1 approximately constitutes the total radiative decay rate. The explicit expression for Γ_1 is presented in [39]. The chip with the qubit is placed in a dilution refrigerator at temperature of 10 mK . In order to provide thermal equilibrium and allow a heterodyne detection of a scattered signal, coaxial wiring with attenuators, isolators, and HEMT amplifiers is assembled. The optical and electron images of the device are depicted in Fig. 1. In the spectroscopic measurements, we probe the qubit transition at low power and observe the Lorentzian dip. The transmitted power is reduced by up to 99% in the exact resonance. We also characterize internal losses and dephasing with the internal Q factor $Q_i \approx 24\,000$ determined with a circle-fit algorithm [40] (also see Supplemental Material [41]).

We prepare the input pulses with a typical heterodyne upconversion setup with rf sources, AWGs (arbitrary waveform generators), and IQ mixers. We ensure $\delta\omega \ll \Gamma_1$. Two sequences of short pulses with carrier frequencies $\omega_\pm$ propagate simultaneously near the qubit. Figure 1 displays an example of a sequence with 6 pulses. The typical pulse duration 5–10 ns guarantees that the qubit keeps coherence while interacting with each light pulse. We also introduce the gap of 2–4 ns in between pulses with different carriers, ensuring no overlap due to some parasitic reflections or rise and fall effects from AWG. This is crucial since mixing of overlapping pulses on a single two-level system gives an entirely different picture of side peaks [33]. The repetition period of 10 μs or more for each sequence allows the qubit to decay freely in between the pulse sequences ensuring the initial ground state before the next pulse sequence with good precision.

We down-convert the scattered light and digitize both quadratures at an intermediate frequency of 100 MHz to characterize the output field. We use high-frequency ADC with an embedded FPGA programmed to average the identical traces recorded when the trigger is sent from AWG. Since we are interested in elastic components, the averaging time is much larger than the period of the sequence. A convenient choice, the time divisible by the period of beats with frequency $2\delta\omega$, allows acquiring all temporal variations of the signal. After recording the complex average field, we make Fourier transformation (FFT) to get the complex spectrum of the signal analyzed below.
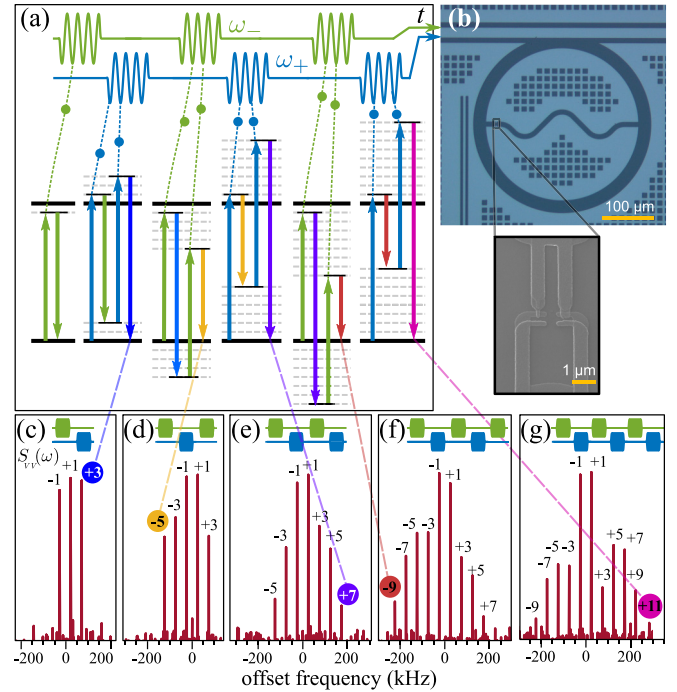

FIG. 1. (a) The sequence of N Rabi pulses scattered on a qubit in the process of QWM. With each additional pulse, a multiphoton process with a pair of photons is emerged. This is illustrated as transitions between dressed levels shifted by $\delta\omega$ from original ones. Therefore the number of elastic peaks is increased with N. (b) The micrograph of the transmon qubit. In the inset, there is the SEM image of the dc squid. (c)–(g) The typical scattering spectra measured for N from 2 to 6, respectively. The processes with $2N$ scattered photons are highlighted in color.

The lower panels of Fig. 1 present a qualitative picture of QWM together with the measured spectra. The leftmost spectrum is obtained for two pulses. The first pulse is at ω_- and the second is at ω_+. Only one side component emerges at ω_{+3} [33]. Adding a third pulse at ω_- results in appearance of two additional components at $\omega_{-3} = 2\omega_- - \omega_+$ and $\omega_{-5} = 2\omega_- - \omega_{+3} = 3\omega_- - 2\omega_+$. The peak at ω_{-5} corresponds to the mixing of six photons (the highest order of mixing for three pulses). It appears when one photon is taken from the first pulse, a pair of photons from a second one, one more pair from the third one, and an extra photon is emitted at ω_{-5}. The fourth pulse at ω_+ would add two more peaks at ω_{+5} and ω_{+7} in a similar scenario. To summarize, N applied pulses enable processes up to $2N$-wave mixing.

To demonstrate that the observed spectral properties are controllable and may alter by time order of driving pulses, we apply three pulses: Two with ω_+ and 8 ns long and one with ω_- 12 ns long; see Fig. 2. The position of ω_+ pulses is fixed, while ω_- pulse is moving. We start with the ω_- pulse being in front of two pulses at ω_+, and finish when the pulse at ω_- is after two pulses at ω_+. We observe a consistent picture of several regimes: (i) three peaks are observed when the negatively detuned pulse is either the first or the last and does not overlap with any of ω_+ pulses; (ii) many peaks (7 or more) are observed when pulses with ω_+ and ω_- overlap; and (iii) five peaks when the pulses are applied one by one as depicted
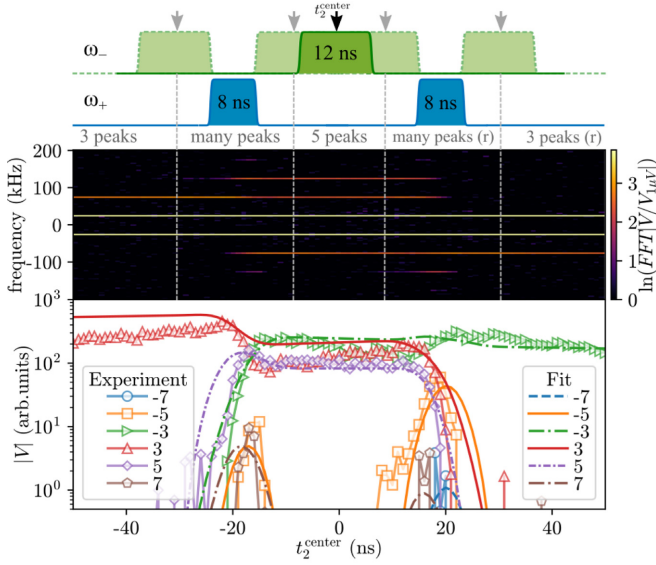
FIG. 2. Upper panel: Sketch of sequence of three pulses: Blue ones are with ω_+ carrier frequency, and the green is with ω_-. Middle panel: The absolute voltage of side components is averaged over many periods of beats and plotted as a function of center position of the middle pulse t_2^{center}. The regions with specific number of components are separated by dashed vertical lines. Bottom panel: The peak amplitudes from the colored graph above are rescaled and plotted along with the numerical simulation results.

at the top panel of Fig 2. Therefore, the temporal configuration of driving pulses controls the qualitative properties of QWM coherent spectrum.

Next, we characterize quantitative properties of side peaks. For that, we measure how durations Δt_-, Δt_+ and amplitudes Ω_-, Ω_+ of pulses affect the intensities of QWM components, implying that similar pulses with the same carrier frequencies rotate qubit states by equal angles. As described earlier, we make complex FFT of down-converted field allowing us to extract amplitude and phase of any coherent component. We also rotate complex traces so that the whole emitted field concentrates in one quadrature and takes either positive or negative values. We plot color maps of these quadratures versus two arguments $\Omega_- \Delta t_-$, $\Omega_+ \Delta t_+$ for each number of pulses N. As a

result, we obtain several expressive maps demonstrating the rich dynamics of fields; see Fig. 3. We interpret the maps by explicitly calculating the evolution of the qubit under a sequence of pulses. Analytical expressions are given for each spectral component.

To interpret the observed elastic spectra in terms of multiphoton scattering, we use the framework developed in [33]. Briefly, we consider two modes of the field c_-, c_+ with frequencies ω_+, ω_- interacting with qubit operators $\sigma_{\pm p}^- \equiv \sigma^- e^{\mp i p \delta \omega t}$, $\sigma_{\pm p}^+ \equiv \sigma^+ e^{\pm i p \delta \omega t}$ which include the phase acquired from the coherent drive.

The Hamiltonian in the interaction picture reads

$$H_\pm = ig(c_\pm^\dagger \sigma_{\pm 1}^- - c_\pm \sigma_{\pm 1}^+). \tag{1}$$

To get the field components, we first calculate the following matrix element which is the expectation value of the operator σ_p^-:

$$M_p^{(N)} = \langle \phi_0 | \Lambda_N^\dagger \sigma_p^- \Lambda_N | \phi_0 \rangle, \tag{2}$$

where the initial state is $|\phi_0\rangle = |0, \gamma_-, \gamma_+\rangle$, meaning that the scattered field mode is initially in the ground state, and the driving fields are always in coherent states $|\gamma_-\rangle$ and $|\gamma_+\rangle$. The interaction with modes happens only when a corresponding pulse reaches the qubit. The evolution operator Λ_N for N applied pulses is defined as

$$\Lambda_N = \prod_{i=1}^N U_{(-1)^i}(\Delta t_i), \tag{3}$$

and evolution operators for every single applied pulse with the duration Δt_i may approximately be expressed in the case of $\gamma_-, \gamma_+ \gg 1$ as

$$U_{\pm 1} \approx \cos\frac{\theta_\pm}{2} + \frac{c_\pm^\dagger \sigma_{\pm 1}^- - c_\pm \sigma_{\pm 1}^+}{\gamma_\pm} \sin\frac{\theta_\pm}{2}. \tag{4}$$

Here we introduced rotation angles $\theta_\pm = \Omega_\pm \Delta t_i$ and used $\Omega_\pm = 2g\gamma_\pm$. For convenience, we also define the following operators:

$$a^\dagger = \alpha c_- \sigma_{-1}^+ / \gamma_-, \quad b^\dagger = \beta c_+ \sigma_{+1}^+ / \gamma_+, \tag{5}$$

where $\alpha = \tan\theta_-/2$, $\beta = \tan\theta_+/2$.

With these expressions, for the case $N = 2$, one obtains

$$M_p^{(2)} = \left(\cos\frac{\theta_+}{2}\cos\frac{\theta_-}{2}\right)^2 \langle \phi_0 | \left(-\underbrace{\sigma_p^- b^\dagger}_{e^{i\delta t}} - \underbrace{\sigma_p^- a^\dagger}_{e^{-i\delta t}} + \underbrace{ab^\dagger \sigma_p^- a^\dagger}_{e^{i\delta t}} + \underbrace{ab^\dagger \sigma_p^- b^\dagger}_{e^{3i\delta t}} \right) |\phi_0\rangle, \tag{6}$$

where under brackets denote the total phase multiplier acquired from operators a, b, $a^\dagger$, $b^\dagger$, not counting the phase of σ_p^- for a moment. If we now calculate the time-average field at an arbitrary frequency ω_p,

$$V_p^{(2)} = -i\frac{\hbar\Gamma_1}{\mu}\frac{1}{T}\int_0^T M_p^{(2)} \, dt, \tag{7}$$

the last term of Eq. (6) will give a nonzero component for $p = 3$, since the phase multiplier from $\sigma_{+3}^- = \sigma^- e^{-3i\delta t}$ can-

cels out the phase picked from operators of driving modes. Therefore we see that the phases underlined in Eq.(6) define the frequencies of nonzero elastic components observed when measuring the field spectrum with a low bandwidth. It explains the leftmost spectrum in Fig. 1 which consists of only three components. We also derive how their amplitude depends on rotation angles:

$$V_3^{(2)} \propto \frac{1}{2}\sin^2\frac{\theta_+}{2}\sin\theta_-. \tag{8}$$
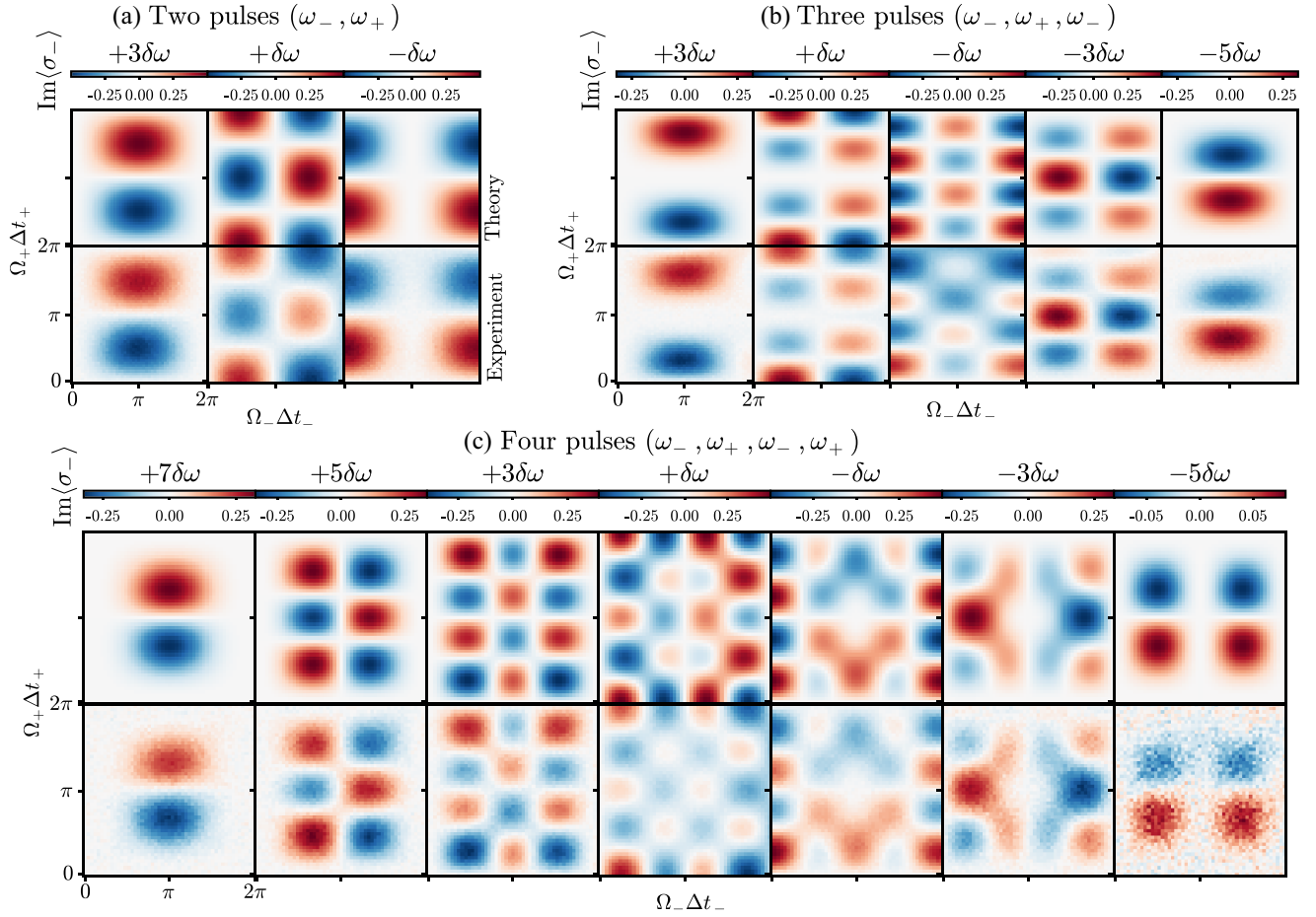
FIG. 3. The heterodyne-measured complex-valued field of all observed side peaks for sequences of N non-overlapping pulses plotted as functions of $\theta_+ = \Omega_+\Delta t_+$ and $\theta_- = \Omega_-\Delta t_-$. The temporal order of pulses is written in parentheses in the title for each group of measurements. The $\Omega_-\Delta t_-$ ($\Omega_+\Delta t_+$) varies along the horizontal (vertical) axis for all ω_- (ω_+) pulses simultaneously. In the experiment, amplitudes Ω_+ and Ω_- were changed, $\delta\omega = 25$ kHz. The unit of the color bar axes is the unit of $\mathrm{Im}\langle\sigma_-\rangle$ and applies to the theoretical plots. Z axis for each experimental plot is rescaled by a common multiplier to fit the theory.

It is now straightforward to generalize the calculation for $N > 2$ pulses. For three pulses, the analog of Eq. (6) also expresses M_p^3 as a sum of terms, and among them there is only the operator term $ba^\dagger\sigma_p^- a^\dagger ba^\dagger$ with acquired phase $e^{-5i\delta t}$, contributing to the peak at ω_{-5}. This peak is highlighted on the second panel from the left in Fig. 1. For the field, we obtain

$$V_{-5}^{(3)} \propto \frac{1}{2}\sin\theta_- \sin^2\frac{\theta_-}{2}\sin^2\frac{\theta_+}{2}. \tag{9}$$

The spectrum of emitted field recorded for different θ_- and θ_+ allows us to reconstruct how every observable harmonic depends on rotation angles. We then compare these results with the corresponding analytical dependencies, similar to Eqs. (8) and (9). Both measured and calculated intensities are presented in Fig. 3 for $2 \leqslant N \leqslant 4$. Supplemental Material [41] contains measured results for $N = 5, 6$. For all measured components, the theory excellently fits experimental maps, even for very high orders. However, we notice a small disagreement for the emission at the frequency of the last pulse (either ω_+ or ω_-) at large effective angles. The origin of this discrepancy could be in our data processing procedure. To restore dependencies for ω_+ and ω_-, we replace the initial pulses with zero in the digitized traces, thus losing a

small part of the emission. Besides, some part of the last pulse might get distorted due to presence of a slight impedance mismatch in the signal line. It may cause a significant effect if the rotation angle is large.

Analyzing the patterns in Fig. 3, we outline several specific features of the observed dependencies. First, we note that at $\theta_- = \theta_+ = \pi$, all components are zero for all values of N. In this case, each pulse is a π pulse; hence the qubit reaches either ground or excited state, does not contain any phase from the pulses, and emits incoherently. Second, when the first pulse is negatively detuned, for all values of N, $\omega_{(4p-1)}$ components are zero at $\theta_+ = \pi$, and the maps are antisymmetrical along the line $\theta_+ = \pi$. Similarly, the maps for $\omega_{(4p-3)}$ components are antisymmetric relative to $\theta_- = \pi$. It implies that at $\theta_- = \pi$ ($\theta_+ = \pi$), there are many values of θ_+ (θ_-), for which emission contains the only component at $\omega_{(4p-3)}$ ($\omega_{(4p-1)}$). Similar nontrivial spectral distribution was recently predicted to appear in QWM of a squeezed vacuum with a coherent field [36]. However, here the origin of missing peaks is due to a pulsed drive.

Our analytical results allow the exact identification of multiphoton contributions into every single mode. As N increases, the higher-order photon processes contribute more signifi-
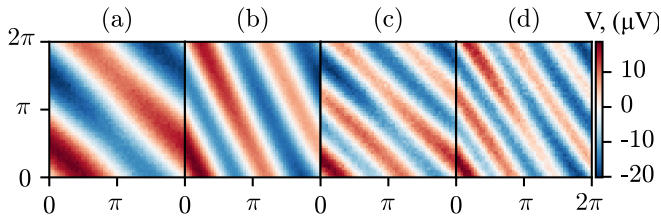
FIG. 4. The net field obtained as a sum of all measured coherent components, as if it could be emitted for the drives with $\delta\omega = 0$, that is, for a monochromatic drive. From (a) to (d) the map is plotted for $N = 2, 3, 4, 5$ pulses; horizontal axis is θ_- and vertical is θ_+. The cross sections are harmonic Rabi oscillations.

cantly to the emission at the frequencies of initial drives and the neighboring frequencies. For example, for $N = 3$, the field at ω_- contains the only term corresponding to a single-photon process (single-photon absorption and emission, or in analogy with higher orders, "two-wave mixing"), two terms related to the third-order processes (four-wave mixing), and one term connected with the fifth-order process (six-wave mixing). The exact expressions are presented in the Supplemental Material [41] . Therefore, the interference of terms with different orders forms the overall pattern for every component. However, there is always a single term in the evolution responsible for the emission at the leftmost and rightmost peak frequencies.

The observed pictures could be considered as a spectral decomposition of coherent pulses being scattered by a qubit. To illustrate the physical meaning of this decomposition, we can consider the limit $\delta\omega \rightarrow 0$. Our interleaved pulses then turn to the continuous monochromatic wave exactly resonant with the

qubit. The side peaks now all have the same frequency, and we can simply sum up all the contributions presented in Fig. 3 for each sequence resulting in simple Rabi dynamics; see Fig. 4. The number of Rabi periods along each axis corresponds to the number of pulses of each kind in a pulse sequence.

Another observation relates to the conversion of frequency components. For example, as can be seen in Fig. 3(a), as a result of mixing two pulses with parameters $\theta_- = \pi$ and $\theta_+ = \pi/2$, the whole coherent field becomes converted into the ω_{+3} mode. Note that there is also incoherently emitted radiation due to inelastic scattering. Correspondingly, for $N > 2$ pulses, the distribution of coherent field among side spectral components is more complicated. Nonetheless, there are also rotation angles where there is only one or two nonzero components.

In summary, we study QWM of light pulses on a single qubit that reveals the intrinsic connection between qubit dynamics and multiphoton processes of elastic scattering. The study of these effects will increase understanding of nonlinear quantum optics with quantum objects playing the role of a scatterer. Recent theoretical efforts show that the wave mixing of classical and quantum fields on a qubit in a waveguide is a good tool for measuring the photon statistics of the quantum signal. However, a qubit itself is also a reliable source of nonclassical radiation when driven continuously or by short pulses. Nontrivial coherent spectra might indicate generation of light with more sophisticated statistics than just squeezing or antibunching. Thus, a promising area opens up for further research of microwave optics and photonics.

[1] C. Cohen-Tannoudji, J. Dupont-Roc, and G. Grynberg, *Atom-Photon Interactions: Basic Processes and Applications*, Claude Cohen-Tannoudji, Jacques Dupont-Rock, & Gilbert Grynberg (John Wiley & Sons, Inc., New York, 1998), p. 656.

[2] P. Meystre and M. Sargent, in *Elements of Quantum Optics* (Springer, Berlin, 1990), pp. 395–424.

[3] D. F. Walls and G. J. Milburn, in *Quantum Optics* (Springer, Berlin, 1994), pp. 213–228.

[4] B. R. Mollow, Phys. Rev. **188**, 1969 (1969).

[5] H. J. Kimble and L. Mandel, Phys. Rev. A **13**, 2123 (1976).

[6] F. Y. Wu, R. E. Grove, and S. Ezekiel, Phys. Rev. Lett. **35**, 1426 (1975).

[7] A. Muller, E. B. Flagg, P. Bianucci, X. Y. Wang, D. G. Deppe, W. Ma, J. Zhang, G. J. Salamo, M. Xiao, and C. K. Shih, Phys. Rev. Lett. **99**, 187402 (2007).

[8] O. Astafiev, A. M. Zagoskin, A. A. Abdumalikov Jr., Y. A. Pashkin, T. Yamamoto, K. Inomata, Y. Nakamura, and J. S. Tsai, Science **327**, 840 (2010).

[9] P. A. Apanasevich and S. J. Kilin, J. Phys. B **12**, L83 (1979).

[10] H. J. Kimble, M. Dagenais, and L. Mandel, Phys. Rev. Lett. **39**, 691 (1977).

[11] C. Matthiesen, A. N. Vamivakas, and M. Atatüre, Phys. Rev. Lett. **108**, 093602 (2012).

[12] C. L. Phillips, A. J. Brash, D. P. S. McCutcheon, J. Iles-Smith, E. Clarke, B. Royall, M. S. Skolnick, A. M. Fox, and A. Nazir, Phys. Rev. Lett. **125**, 043603 (2020).

[13] L. Hanschke, L. Schweickert, J. C. L. Carreño, E. Schöll, K. D. Zeuner, T. Lettner, E. Z. Casalengua, M. Reindl, S. F. C. Da Silva, R. Trotta, J. J. Finley, A. Rastelli, E. del Valle, F. P. Laussy, V. Zwiller, K. Müller, and K. D. Jöns, Phys. Rev. Lett. **125**, 170402 (2020).

[14] D. F. Walls and P. Zoller, Phys. Rev. Lett. **47**, 709 (1981).

[15] W. Vogel, Phys. Rev. Lett. **67**, 2450 (1991).

[16] M. Collett, D. Walls, and P. Zoller, Opt. Commun. **52**, 145 (1984).

[17] C. H. Schulte, J. Hansom, A. E. Jones, C. Matthiesen, C. Le Gall, and M. Atatüre, Nature (London) **525**, 222 (2015).

[18] R. Short and L. Mandel, Phys. Rev. Lett. **51**, 384 (1983).

[19] A. Aspect, G. Roger, S. Reynaud, J. Dalibard, and C. Cohen-Tannoudji, Phys. Rev. Lett. **45**, 617 (1980).

[20] G. Nienhuis, Phys. Rev. A **47**, 510 (1993).

[21] P. Y. Wen, A. F. Kockum, H. Ian, J. C. Chen, F. Nori, and I.-C. Hoi, Phys. Rev. Lett. **120**, 063603 (2018).

[22] Y. Zhu, Q. Wu, A. Lezama, D. J. Gauthier, and T. W. Mossberg, Phys. Rev. A **41**, 6574 (1990).

[23] M. Peiris, K. Konthasinghe, Y. Yu, Z. C. Niu, and A. Muller, Phys. Rev. B **89**, 155305 (2014).

[24] J. Pan, H. Z. Jooya, G. Sun, Y. Fan, P. Wu, D. A. Telnov, S.-I. Chu, and S. Han, Phys. Rev. B **96**, 174518 (2017).

[25] S. P. Tewari and M. K. Kumari, Phys. Rev. A **41**, 5273 (1990).

[26] Z. Ficek and H. S. Freedhoff, Phys. Rev. A **48**, 3092 (1993).

[27] G. S. Agarwal, Y. Zhu, D. J. Gauthier, and T. W. Mossberg, J. Opt. Soc. Am. B **8**, 1163 (1991).

[28] H. Freedhoff and Z. Chen, Phys. Rev. A **41**, 6013 (1990).

[29] W. M. Ruyten, J. Opt. Soc. Am. B **9**, 1892 (1992).

[30] U. Leonhardt and H. Paul, Phys. Rev. A **48**, 4598 (1993).

[31] A. A. Abdumalikov, O. V. Astafiev, Y. A. Pashkin, Y. Nakamura, and J. S. Tsai, Phys. Rev. Lett. **107**, 043604 (2011).

[32] Y. Lu, A. Bengtsson, J. J. Burnett, E. Wiegand, B. Suri, P. Krantz, A. F. Roudsari, A. F. Kockum, S. Gasparinetti, G. Johansson *et al.*, npj Quantum Inf. **7**, 35 (2021).

[33] A. Y. Dmitriev, R. Shaikhaidarov, V. N. Antonov, T. Hönigl-Decrinis, and O. V. Astafiev, Nat. Commun. **8**, 1352 (2017).

[34] A. Y. Dmitriev, R. Shaikhaidarov, T. Hönigl-Decrinis, S. E. de Graaf, V. N. Antonov, and O. V. Astafiev, Phys. Rev. A **100**, 013808 (2019).

[35] T. Hönigl-Decrinis, R. Shaikhaidarov, S. E. de Graaf, V. N. Antonov, and O. V. Astafiev, Phys. Rev. Appl. **13**, 024066 (2020).

[36] W. V. Pogosov, A. Y. Dmitriev, and O. V. Astafiev, Phys. Rev. A **104**, 023703 (2021).

[37] J. Koch, T. M. Yu, J. Gambetta, A. A. Houck, D. I. Schuster, J. Majer, A. Blais, M. H. Devoret, S. M. Girvin, and R. J. Schoelkopf, Phys. Rev. A **76**, 042319 (2007).

[38] M. D. Hutchings, J. B. Hertzberg, Y. Liu, N. T. Bronn, G. A. Keefe, M. Brink, J. M. Chow, and B. L. T. Plourde, Phys. Rev. Appl. **8**, 044003 (2017).

[39] A. Vasenin, A. Dmitriev, S. Kadyrmetov, and O. Astafiev, in *Fifth International Conference on Quantum Technologies (ICQT-2019)*, edited by A. Fedorov and A. Rubtsov, AIP Conf. Proc. No. 2241 (AIP, New York, 2020), p. 020036.

[40] S. Probst, F. B. Song, P. A. Bushev, A. V. Ustinov, and M. Weides, Rev. Sci. Instrum. **86**, 024706 (2015).

[41] See Supplemental Material at http://link.aps.org/supplemental/10.1103/PhysRevA.106.L041701 for details on the sample fabrication, measurement setup, spectroscopy and dynamical properties of the transmon qubit, analytical calculations and experimental data with 5 and 6 pulses in a pulse sequence.